


# Near-field radiative heat transfer between nanoporous GaN films

Xiaozheng Han(韩晓政), Jihong Zhang(张纪红), Haotuo Liu(刘皓佗), Xiaohu Wu(吴小虎), and Huiwen Leng(冷惠文)

**Citation:**Chin. Phys. B, 2024, 33 (**4**): 047801. DOI: 10.1088/1674-1056/ad09a9
Journal homepage: http://cpb.iphy.ac.cn; http://iopscience.iop.org/cpb

**What follows is a list of articles you may be interested in**

78.20.-e

---

## Probing photocarrier dynamics of pressurized graphene using time-resolved terahertz spectroscopy

Yunfeng Wang(王云峰), Shujuan Xu(许淑娟), Jin Yang(杨金), and Fuhai Su(苏付海)
Chin. Phys. B, 2023, 32 (**6**): 067802. DOI: 10.1088/1674-1056/acc2b1

## Atomic-scale insights of indium segregation and its suppression by GaAs insertion layer in InGaAs/AlGaAs multiple quantum wells

Shu-Fang Ma(马淑芳), Lei Li(李磊), Qing-Bo Kong(孔庆波), Yang Xu(徐阳), Qing-Ming Liu(刘青明), Shuai Zhang(张帅), Xi-Shu Zhang(张西数), Bin Han(韩斌), Bo-Cang Qiu(仇伯仓), Bing-She Xu(许并社), and Xiao-Dong Hao(郝晓东)
Chin. Phys. B, 2023, 32 (**3**): 037801. DOI: 10.1088/1674-1056/ac70b5

## Acoustic plasmonics of Au grating/$Bi_2Se_3$ thin film/sapphirehybrid structures

Weiwu Li(李伟武), Konstantin Riegel, Chuanpu Liu(刘传普), Alexey Taskin, Yoichi Ando, Zhimin Liao(廖志敏), Martin Dressel, Yuan Yan(严缘)
Chin. Phys. B, 2020, 29 (**6**): 067801. DOI: 10.1088/1674-1056/ab8a3c

## Extinction mechanisms of hyperbolic h-BN nanodisk

Runkun Chen(陈闰堃), Jianing Chen(陈佳宁)
Chin. Phys. B, 2020, 29 (**5**): 057802. DOI: 10.1088/1674-1056/ab8898

## Numerical investigation of the enhanced unidirectional surface plasmon polaritons generator

Zhang Zhi-Dong (张志东), Wang Hong-Yan (王红艳), Zhang Zhong-Yue (张中月), Wang Hui (王辉)
Chin. Phys. B, 2014, 23 (**1**): 017801. DOI: 10.1088/1674-1056/23/1/017801

---

**SPECIAL TOPIC — Heat conduction and its related interdisciplinary areas**

# Near-field radiative heat transfer between nanoporous GaN films

Xiaozheng Han(韩晓政)[1], Jihong Zhang(张纪红)[1], Haotuo Liu(刘皓佗)[2], Xiaohu Wu(吴小虎)[3,†], and Huiwen Leng(冷惠文)[1,‡]

[1] *School of Electromechanical and Automotive Engineering, Yantai University, Yantai* 264005, *China*
[2] *Key Laboratory of Advanced Manufacturing and Intelligent Technology, Ministry of Education, Harbin University of Science and Technology, Harbin* 150080, *China*
[3] *Thermal Science Research Center, Shandong Institute of Advanced Technology, Jinan* 250100, *China*

(Received 9 August 2023; revised manuscript received 20 October 2023; accepted manuscript online 4 November 2023)

Photon tunneling effects give rise to surface waves, amplifying radiative heat transfer in the near-field regime. Recent research has highlighted that the introduction of nanopores into materials creates additional pathways for heat transfer, leading to a substantial enhancement of near-field radiative heat transfer (NFRHT). Being a direct bandgap semiconductor, GaN has high thermal conductivity and stable resistance at high temperatures, and holds significant potential for applications in optoelectronic devices. Indeed, study of NFRHT between nanoporous GaN films is currently lacking, hence the physical mechanism for adding nanopores to GaN films remains to be discussed in the field of NFRHT. In this work, we delve into the NFRHT of GaN nanoporous films in terms of gap distance, GaN film thickness and the vacuum filling ratio. The results demonstrate a 27.2% increase in heat flux for a 10 nm gap when the nanoporous filling ratio is 0.5. Moreover, the spectral heat flux exhibits redshift with increase in the vacuum filling ratio. To be more precise, the peak of spectral heat flux moves from $\omega = 1.31 \times 10^{14}$ rad·s$^{-1}$ to $\omega = 1.23 \times 10^{14}$ rad·s$^{-1}$ when the vacuum filling ratio changes from $f = 0.1$ to $f = 0.5$; this can be attributed to the excitation of surface phonon polaritons. The introduction of graphene into these configurations can highly enhance the NFRHT, and the spectral heat flux exhibits a blueshift with increase in the vacuum filling ratio, which can be explained by the excitation of surface plasmon polaritons. These findings offer theoretical insights that can guide the extensive utilization of porous structures in thermal control, management and thermal modulation.

**Keywords:** near-field radiative heat transfer, nanoporous GaN film, surface phonon polaritons, surface plasmon polaritons

**PACS:** 78.20.–e, 71.36.+c, 78.20.Bh **DOI:** 10.1088/1674-1056/ad09a9

## 1. Introduction

In recent decades, a plethora of experimental and theoretical studies have confirmed that in the near-field regime the photon tunneling effect, driven by evanescent waves, can defy the black-body radiation law and amplify near-field radiative heat transfer (NFRHT) between bodies,[1–26] particularly when coupling modes between surface waves, including surface plasmon polaritons (SPPs) and surface phonon polaritons (SPhPs), come into play. The boosted NFRHT holds significant promise in diverse practical applications,[27,28] including thermal energy conversion,[29,30] radiative cooling[31–33] and advances in thermophotovoltaics.[34–37] However, the effective control of NFRHT across different application domains continues to pose a persistent challenge.

In the quest for enhanced NFRHT, scientists have investigated intricate configurations, unique materials and innovative techniques with the aim of pushing the boundaries of this phenomenon. For instance, the exploration of materials has evolved from the realm of isotropic materials to the intricate domain of anisotropic materials, capable of exciting hyperbolic polaritons using effective medium theory (EMT).[38–45] In recent years, a vacuum has been incorporated into both two-body and three-body systems to boost NFRHT. Biehs *et al.*[46] have investigated NFRHT between two nanoporous materials, demonstrating that air inclusion significantly enhances the near-field radiative heat flux (NFRHF). Liu *et al.*[47] have studied a doped silicon nanohole (D-SiNH) structure and observed that the heat transfer coefficient between D-SiNHs is 11.3 times higher than that of doped silicon bulk when the fraction of doped silicon is $f = 1 - \pi/4$ with a 10 nm gap. Prior research has indicated that nanowire arrays facilitate photon tunneling in a hyperbolic characteristic mode, exerting a significant influence on NFRHT. In their study, Hong *et al.*[48] have showcased a graphene-covered SiC nanowire array (NWA) model supporting hyperbolic modes, revealing that the NFRHF between graphene-covered SiC NWAs surpasses that between graphene-covered SiC bulks, especially at a wider vacuum gap. Moreover, the effects of nanopores on NFRHT are not only relevant in two-body systems but also in three-body systems. Li *et al.*[49] conducted an investigation on NFRHT in a three-body system comprising nanoporous SiC, and found that the filling factor exerts a substantial influence

†Corresponding author. E-mail: xiaohu.wu@iat.cn
‡Corresponding author. E-mail: lenghw86_2022@qq.com

© 2024 Chinese Physical Society and IOP Publishing Ltd 

on NFRHT. Hence, investigation of nanoporous materials with the aim of enhancing NFRHT is an interesting and valuable area for exploration.

Gallium nitride (GaN), a third-generation wide-bandgap semiconductor material, boasts high thermal conductivity, stable high-temperature resistance and excellent mechanical properties, making it valuable for optoelectronic device applications.[50–52] The performance of nanoporous GaN surpasses that of GaN bulk in terms of luminescence,[53] leading to widespread interest from researchers investigating luminescence. Nevertheless, there have been few investigations focused on NFRHT involving nanoporous GaN thin films.[54] The fundamental physical mechanisms behind this phenomenon warrant in-depth research.

As a two-dimensional crystal material, graphene exhibits outstanding electrical and optical properties. Graphene has been proven to support SPPs in the range from terahertz to near-infrared frequencies.[28] Importantly, the SPPs supported by graphene can be tuned through chemical doping or gate voltage modulation.[55,56] These properties of graphene create excellent prospects for its utilization in areas of NFRHT. As a consequence, it is worth studying the NFRHT between nanoporous GaN films covered by graphene to further enhance radiative heat transfer in the near-field regime.

Here, we investigate NFRHT in a porous configuration composed of GaN film with and without graphene. The structure can be modulated by means of changing the gap distance, the thickness of GaN film and the vacuum filling ratio. The NFRHF in such a nanoporous GaN structure can be enhanced in contrast with that in the corresponding GaN structure without nanopores. Moreover, our findings reveal that the peak frequency of the spectral heat flux (SHF) can be controlled by adjusting the vacuum filling ratio. The excitation of SPhPs and SPPs is analyzed from the distribution of energy transmission coefficients. Gaining insights into the physical mechanisms behind NFRHT among nanoporous GaN films is important for advances in thermal imaging, radiative cooling and thermal management utilizing nanoporous materials.

## 2. Theoretical model

GaN is characterized by uniaxial anisotropy, and previous studies have demonstrated its significant absorption properties related to SPhPs.[57–60] Figure 1(a) depicts a theoretical model comprising two semi-infinite GaN films, and this configuration is referred to as the GaN structure. Figure 1(b) presents the NFRHT model involving nanoporous GaN films, identified as the nanoporous GaN structure. Additionally, in the context of the model, $d$ signifies the vacuum gap, $d_{\mathrm{h}}$ denotes the thickness of both GaN and nanoporous GaN films, while $T_1$ and $T_2$ indicate the temperatures of the emitter and receiver, respectively. In the calculation, we fix $T_1 = 400$ K and $T_2 = 300$ K.

The permittivity of GaN can be given as[61]

$$\varepsilon_{\perp(\parallel)}(\omega) = \varepsilon_{\infty,\perp(\parallel)}\left(\frac{\omega^2_{\mathrm{LO},\perp(\parallel)} - \omega^2 - \mathrm{i}\omega\gamma_{\mathrm{LO},\perp(\parallel)}}{\omega^2_{\mathrm{TO},\perp(\parallel)} - \omega^2 - \mathrm{i}\omega\gamma_{\mathrm{TO},\perp(\parallel)}}\right). \quad (1)$$

The physical parameters of GaN are as follows: $\varepsilon_{\infty,\perp} = 5.14$, $\omega_{\mathrm{LO},\perp} = 740.6$ cm$^{-1}$, $\gamma_{\mathrm{LO},\perp} = 7.0$ cm$^{-1}$, $\omega_{\mathrm{TO},\perp} = 561.0$ cm$^{-1}$, $\gamma_{\mathrm{TO},\perp} = 5.9$ cm$^{-1}$, $\varepsilon_{\infty,\parallel} = 5.31$, $\omega_{\mathrm{LO},\parallel} = 734.7$ cm$^{-1}$, $\gamma_{\mathrm{LO},\parallel} = 6.8$ cm$^{-1}$, $\omega_{\mathrm{TO},\parallel} = 538.4$ cm$^{-1}$, and $\gamma_{\mathrm{TO},\parallel} = 5.9$ cm$^{-1}$. Based on Eq. (1), the real components of the permittivity of GaN are shown in Fig. 2(a).

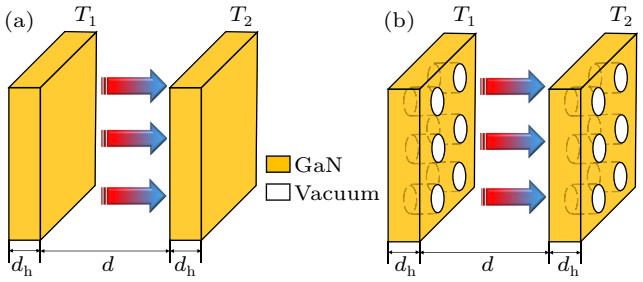



**Fig. 1.** (a) Near-field radiative heat transfer model of a GaN structure. (b) Near-field radiative heat transfer model of a nanoporous GaN structure.

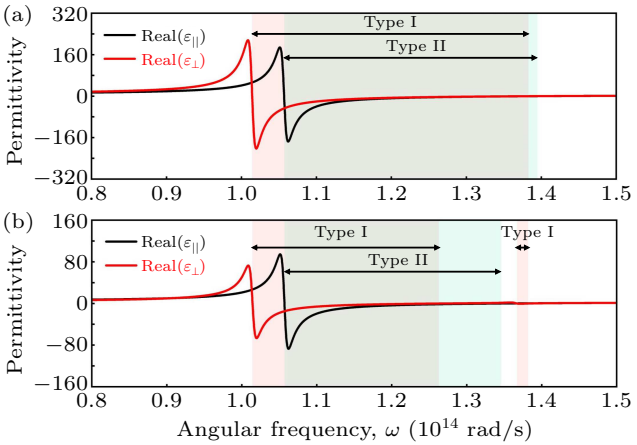



**Fig. 2.** (a) The real permittivity of GaN. (b) The real permittivity of nanoporous GaN with $f = 0.5$. The red and green regions denote type I and type II HBs, respectively.

The limit of validity of EMT in the near-field regime is restricted to $d \gg a/\pi$, where $d$ is the gap distance and $a$ is the lattice constant of the nanoporous GaN. The EMT can be employed for distances $d$ between 10 nm and 1000 nm in the small structures of chemically generated nanoporous materials.[46] When the gap distance $d$ is 10 nm, the lattice constant of the nanopores should not exceed 30 nm in the structures. Hence, we only consider filling fractions $f$ ranging from 0.0 to 0.5, which is the same as that considered in Ref. [46]. The size of the nanopores should be no more than 30 nm. Based on EMT, the permittivity of nanoporous GaN is given as[46]

$$\varepsilon_{\parallel}(\omega) = \varepsilon_{\mathrm{n},\parallel}(\omega)\frac{\varepsilon_{\mathrm{m}}(1+f) + \varepsilon_{\mathrm{n},\parallel}(\omega)(1-f)}{\varepsilon_{\mathrm{m}}(1-f) + \varepsilon_{\mathrm{n},\parallel}(\omega)(1+f)}, \quad (2)$$

$$\varepsilon_{\perp}(\omega) = f\varepsilon_{\mathrm{m}} + (1-f)\varepsilon_{\mathrm{n},\perp}(\omega), \quad (3)$$

where $\varepsilon_{\rm n}$ denotes the permittivity of GaN, which is obtained from Eq. (1). $\varepsilon_{\rm m}$ denotes the vacuum dielectric function and $\varepsilon_{{\rm m},\perp}=\varepsilon_{{\rm m},\parallel}=1$. The vacuum filling ratio is denoted by $f$, and the permittivity of nanoporous GaN with $f=0.5$ is shown in Fig. 2(b). The shaded area delineates two distinct hyperbolic bands (HBs): the type I HB characterized by $\varepsilon_\perp>0$ and $\varepsilon_\parallel<0$, marked in red, and the type II HB denoted by $\varepsilon_\perp<0$ and $\varepsilon_\parallel>0$, highlighted in green. In addition, the overlapping shaded region is the overlapping HB with $\varepsilon_\perp<0$ and $\varepsilon_\parallel<0$.

In accordance with the fluctuation-dissipation theorem and the dyadic Green's function, the near-field radiation heat flux $Q$ between two semi-infinite plates with different temperatures $T_1$ and $T_2$ is calculated using the following equation when the vacuum gap is $d$:[62,63]

$$Q=\frac{1}{4\pi^2}\int_0^\infty\left[\theta\left(\omega,T_1\right)-\theta\left(\omega,T_2\right)\right]\mathrm{d}\omega\times\int_0^\infty\xi_{j=\mathrm{s,p}}\left(\omega,\beta\right)\beta\,\mathrm{d}\beta,\tag{4}$$

where $\omega$ denotes the angular frequency, $\beta$ refers to the transverse component of the wave vector, $\theta(\omega,T)$ represents the average energy of the Planck harmonic oscillator, which can be computed using

$$\theta\left(\omega,T\right)=\frac{\hbar\omega}{\exp\left(\frac{\hbar\omega}{k_{\rm B}T}\right)-1},\tag{5}$$

where $\hbar=h/(2\pi)$ symbolizes the reduced Planck constant, $h$ denotes Planck's constant ($h=6.626\times10^{-34}$ J·s), $k_{\rm B}$ stands for Boltzmann's constant ($k_{\rm B}=1.381\times10^{-23}$ J·K$^{-1}$) and $\xi_{j=\mathrm{s,p}}(\omega,\beta)$ signifies the energy transmission coefficient. The energy transmission coefficient incorporates the contributions of both propagated waves ($\beta<k_0$) and evanescent waves ($\beta>k_0$). Specifically, it can be expressed as the sum of $\xi_{j=\mathrm{s,p}}(\omega,\beta)=\xi_{\rm s}(\omega,\beta)+\xi_{\rm p}(\omega,\beta)$,[64] and is calculated by

$$\xi_{j=\mathrm{s,p}}\left(\omega,\beta\right)=\begin{cases}\dfrac{\left(1-\left|r_{j,\mathrm{E}}\right|^2\right)\left(1-\left|r_{j,\mathrm{R}}\right|^2\right)}{\left|1-r_{j,\mathrm{E}}r_{j,\mathrm{R}}\,\mathrm{e}^{2\mathrm{i}k_{z0}d}\right|^2}, & \beta<k_0,\\[2ex]\dfrac{4\mathrm{Im}\left(r_{j,\mathrm{E}}\right)\mathrm{Im}\left(r_{j,\mathrm{E}}\right)\mathrm{e}^{2\mathrm{i}k_{z0}d}}{\left|1-r_{j,\mathrm{E}}r_{j,\mathrm{R}}\,\mathrm{e}^{2\mathrm{i}k_{z0}d}\right|^2}, & \beta>k_0,\end{cases}\tag{6}$$

where $r_{j,\mathrm{E}}$ signifies the Fresnel reflection coefficient from vacuum to emitter and $r_{j,\mathrm{R}}$ represents the Fresnel reflection coefficient from vacuum to receiver. $e$ signifies the elementary charge and i stands for the imaginary unit. Note that $k_{z0}$ is the component in the vertical-component wavevector in the vacuum and $k_{z0}=\sqrt{k_0^2-\beta^2}$. $k_0$ is the wavevector in the vacuum, calculated as $k_0=\omega/c_0$, where $c_0$ is the speed of light in a vacuum.

The Fresnel reflection coefficients between two semi-infinite media can be calculated using[65]

$$r_{\rm s}=\frac{k_z^{(0\mathrm{s})}-k_z^{(1\mathrm{s})}}{k_z^{(0\mathrm{s})}+k_z^{(1\mathrm{s})}},\tag{7}$$

$$r_{\rm p}=\frac{k_z^{(0\mathrm{p})}\varepsilon_\perp^{(1)}-k_z^{(1\mathrm{p})}\varepsilon_\perp^{(0)}}{k_z^{(0\mathrm{p})}\varepsilon_\perp^{(1)}+k_z^{(1\mathrm{p})}\varepsilon_\perp^{(0)}}.\tag{8}$$

When dealing with a medium of finite thickness, the Fresnel reflection coefficients are calculated using[1,3]

$$r_{\rm s}=\frac{r_{\rm s01}+r_{\rm s12}\left(1+r_{\rm s01}+r_{\rm s10}\right)\mathrm{e}^{2\mathrm{i}k_z^{(1\mathrm{s})}d_{\rm h}}}{1-r_{\rm s01}r_{\rm s12}\,\mathrm{e}^{2\mathrm{i}k_z^{(1\mathrm{s})}d_{\rm h}}},\tag{9}$$

$$r_{\rm p}=\frac{r_{\rm p01}+r_{\rm p12}\left(1-r_{\rm p01}-r_{\rm p10}\right)\mathrm{e}^{2\mathrm{i}k_z^{(1\mathrm{p})}d_{\rm h}}}{1-r_{\rm p01}r_{\rm p12}\,\mathrm{e}^{2\mathrm{i}k_z^{(1\mathrm{p})}d_{\rm h}}},\tag{10}$$

where $k_z^{(n\mathrm{p})}=\sqrt{\varepsilon_\perp^{(n)}k_0^2-\varepsilon_\perp^{(n)}\beta^2/\varepsilon_\parallel^{(n)}}$, $k_z^{(n\mathrm{s})}=\sqrt{\varepsilon_\perp^{(n)}k_0^2-\beta^2}$, $n=0$, 1, 2 refers to the layer number, with 0 and 2 representing the vacuum layers and $\varepsilon_\perp^{(n)}$ and $\varepsilon_\parallel^{(n)}$ represent the dielectric functions of anisotropic materials perpendicular to and parallel to the optical axis, respectively. $d_{\rm h}$ is the thickness of the GaN and $r_{(j=\mathrm{s,p}),n_1,n_2}$ represents the Fresnel reflection coefficient from medium $n_1$ to medium $n_2$.

## 3. Results and discussion

Figure 3(a) illustrates the heat flux $Q$ plotted against gap distance for both GaN and nanoporous GaN, ranging from $f=0.1$ to $f=0.5$ at $d_{\rm h}=50$ nm. One can see that in Fig. 3(a) the NFRHF of these six structures decreases as the gap distance increases, with more significant variations observed among different structures at smaller gap distances. Specifically, at a gap distance of $d=10$ nm, the NFRHF for GaN measures $2.72\times10^6$ W·m$^{-2}$, while for nanoporous GaN with $f=0.1$ it is $3.47\times10^6$ W·m$^{-2}$, signifying an enhancement rate of 27.6%. The NFRHF of nanoporous GaN with $f=0.5$ ($Q=3.46\times10^6$ W·m$^{-2}$) exceeds that of GaN, showing a notable enhancement rate of 27.2%. We have identified the optimal $f$ in relation to changing gap distance, as depicted in Fig. 3(b), highlighting its distinct changes, especially in small gaps of less than 50 nm. The optimal $f$ is 0.1, 0.2, 0.1 and 0.1 when the gap distance $d=10$ nm, 20 nm, 30 nm and 40 nm, respectively. When the gap distance increases from 50 nm to 100 nm, the optimal $f$ is 0.5. The parameter on the right coordinate, representing the ratio of maximum heat flux to minimum heat flux, reaches its peak at 1.57 when $d=10$ nm, underscoring the substantial impact of $f$ on NFRHT for smaller gap distances.

The SHF, $Q_\omega$, displays considerable disparities across the three distinct filling ratios. As shown in Fig. 4(a) when $d=10$ nm, the peak of SHF in GaN (solid black line) is situated at $1.34\times10^{14}$ rad·s$^{-1}$ in the HB, and the SHF (solid red line) displays two peaks in the HB region for nanoporous GaN with $f=0.1$, with the left higher peak being located at $1.31\times10^{14}$ rad·s$^{-1}$ in Fig. 4(b), indicating a slight redshift

of SHF when the addition of nanopores to GaN films. The peak of SHF continues to redshift at $1.23 \times 10^{14}$ rad·s$^{-1}$ (solid blue line) in the HB when $f = 0.5$ (Fig. 4(c)). These phenomena indicate that the SHF shifts to a lower angular frequency with increasing filling factor. When the gap distance is 50 nm, redshifts of the SHF can also be observed as dotted lines in Fig. 4. Moreover, the SHF is predominantly concentrated in the region of the HB, where permittivity in both in-plane and out-of-plane directions is negative. In the HBs (shaded in red and green), the value of SHF is relatively low. Specifically, the SHF values in Figs. 4(a)–4(c) are primarily influenced by excitations occurring within the HBs of both $\varepsilon_\perp < 0$ and $\varepsilon_\parallel < 0$, while smaller SHF values are observed in HBs with $\varepsilon_\perp < 0$ ($\varepsilon_\parallel > 0$) or $\varepsilon_\parallel < 0$ ($\varepsilon_\perp > 0$). As a consequence, the NFRHT is mainly contributed by the SHF in HBs of both $\varepsilon_\perp < 0$ and $\varepsilon_\parallel < 0$.

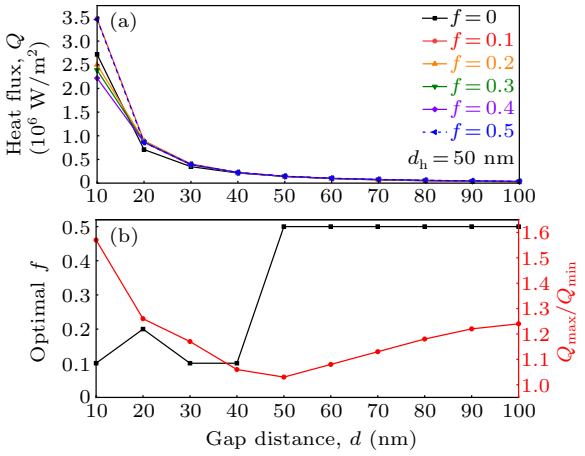



**Fig. 3.** (a) Radiative heat flux as a function of gap distance from 10 nm to 100 nm with $f$ changing from 0 to 0.5. (b) The optimal $f$ as a function of gap distance from 10 nm to 100 nm, and the ratio varying with gap distance.

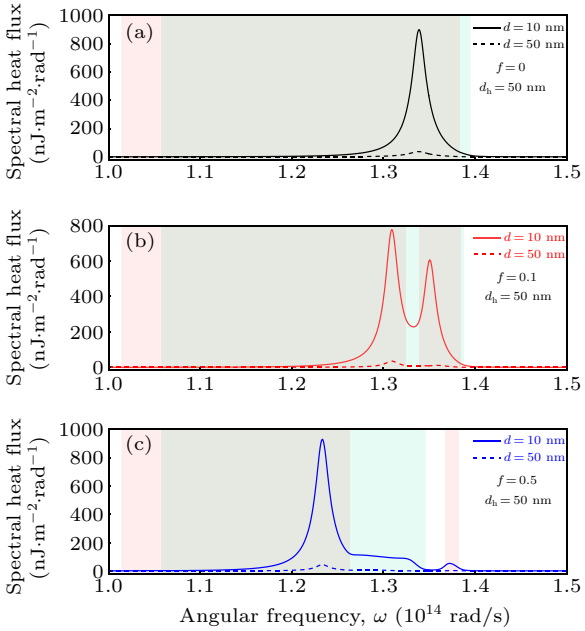



**Fig. 4.** SHF of the three structures at $d = 10$ nm and $d = 50$ nm. The red and green frequency regions denote type I and type II HBs, respectively.

To further assess the impact of each configuration on NFRHT, figures 5(a)–5(f) illustrate the energy transmission coefficients of the three structures at gap distances of 10 nm and 50 nm, respectively. It is evident that the illuminated area diminishes as the gap distance transitions from $d = 10$ nm to $d = 50$ nm, which leads to a decrease in the NFRHF. As shown in Figs. 5(a)–5(c), by increasing the filling factor the SPhP mode supported by GaN moves to a lower angular frequency, aligning well with the redshift observed in the SHF in Fig. 4. Moreover, the SPhP mode splits into two peaks in Fig. 5(b) within the HB, resulting in two peaks of SHF in Fig. 4(b). In Fig. 5(c), the SPhP mode is mainly excited in the HB of both $\varepsilon_\perp < 0$ and $\varepsilon_\parallel < 0$, and the HPPs mode is slightly excited in the HB with $\varepsilon_\perp < 0$ ($\varepsilon_\parallel > 0$) or $\varepsilon_\parallel < 0$ ($\varepsilon_\perp > 0$), in good agreement with distribution of SHF in Fig. 4(c). In particular, the SPhP mode exhibits a more complex behavior with multiple branches when compared with $f = 0.5$ and $f = 0.1$. When $d = 50$ nm, comparable progression of the SPhP mode and HPPs mode can also be found in Figs. 5(d)–5(f). It is obvious in Fig. 5 that the SPhP mode in the HBs of both $\varepsilon_\perp < 0$ and $\varepsilon_\parallel < 0$ is excited most strongly, indicating that the SPhP mode predominantly contributes to the heat flux between nanoporous GaN structures in the near-field.

Figure 6 illustrates the variation of NFRHF with thickness of the GaN thin film for different GaN structures at $d = 20$ nm. As can be seen from Fig. 6, when the thickness of the GaN increases, the heat flux of nanoporous GaN reaches an optimal value and eventually stabilizes at higher levels, surpassing that of GaN without nanopores. Specifically, the NFRHF of GaN reaches a peak at $8.79 \times 10^5$ W·m$^{-2}$ for $d_h = 19$ nm, while the maximum NFRHF value for nanoporous GaN with $f = 0.1$ is $9.05 \times 10^5$ W·m$^{-2}$ when $d_h = 33$ nm. For nanoporous GaN with $f = 0.5$, the NFRHF reaches its highest value of $9.42 \times 10^5$ W·m$^{-2}$ when $d_h = 12$ nm.

Figure 7 illustrates the SHF of three strucutres at varying film thicknesses: $d_h = 10$ nm, $d_h = 20$ nm and $d_h = 30$ nm. As seen, when $f = 0$ in Fig. 7(a), the SHF exhibits two peaks within the HB for $d_h = 10$ nm, while a prominent peak in SHF is evident for $d_h = 20$ nm and $d_h = 30$ nm. With increase in $d_h$ from 20 nm to 30 nm, the peak shape becomes taller and more slender. When $f = 0.1$ in Fig. 7(b), two peaks are located in the HB with both $\varepsilon_\perp < 0$ and $\varepsilon_\parallel < 0$, with the left SHF peak being the highest for $d_h = 20$ nm and the value of the right peak increasing when $d_h$ increases from 10 nm to 30 nm. Simultaneously, the SHF value in the HB with $\varepsilon_\perp < 0$ ($\varepsilon_\parallel > 0$) or $\varepsilon_\parallel < 0$ ($\varepsilon_\perp > 0$) is smaller than in the HBs with both $\varepsilon_\perp < 0$ and $\varepsilon_\parallel < 0$ in Fig. 7(b). Furthermore, the primary contribution to SHF occurs in the HB with both $\varepsilon_\perp < 0$ and $\varepsilon_\parallel < 0$ when $f = 0.5$ in Fig. 7(c), while minimal SHF is observed in HBs with $\varepsilon_\perp < 0$ ($\varepsilon_\parallel > 0$) or $\varepsilon_\parallel < 0$ ($\varepsilon_\perp > 0$).

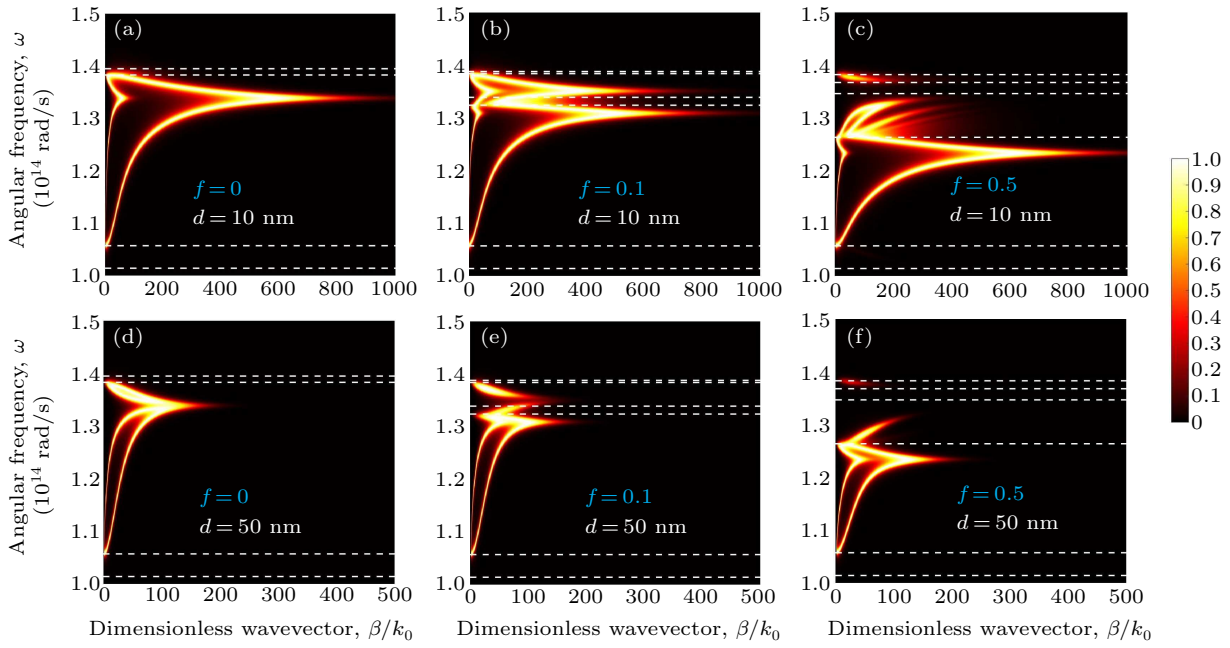



**Fig. 5.** Energy transmission coefficients of GaN and nanoporous GaN with $f = 0.1$ and $f = 0.5$ at $d = 10$ nm and $d = 50$ nm.

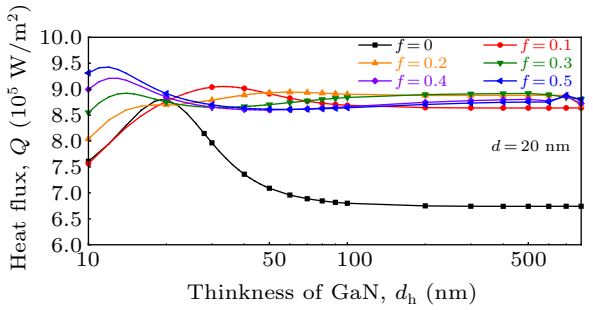



**Fig. 6.** Radiative heat flux as a function of the thickness of GaN thin film for GaN and nanoporous GaN from $f = 0.1$ to $f = 0.5$ at $d = 20$ nm.

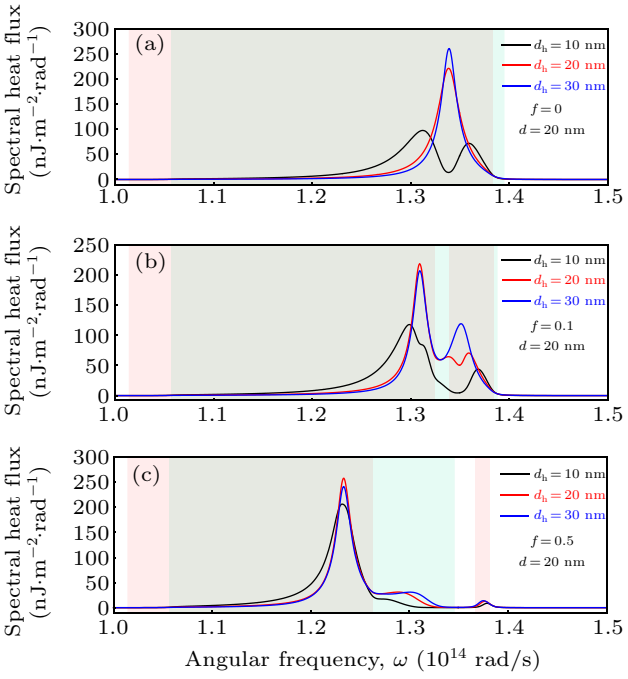



**Fig. 7.** SHF of the three structures at $d_h = 10$ nm, $d_h = 20$ nm and $d_h = 30$ nm.

To delve deeper into the underlying physical mechanisms, we present the energy transmission coefficients of the three structures for GaN film thicknesses $d_h = 10$ nm, $d_h = 20$ nm and $d_h = 30$ nm in Fig. 8. First, one can see in Figs. 8(a)–8(c) that the prominent band corresponds to the SPhP mode predominantly situated in HBs of both $\varepsilon_\perp < 0$ and $\varepsilon_\parallel < 0$. In particular, there is no overlap between two bright bands in Fig. 8(a), signifying the presence of two adjacent peaks in the SHF observed in Fig. 7(a) for $d_h = 10$ nm. In Figs. 8(b) and 8(c), two bright bands overlap, resulting in one SHF peak in Fig. 7(a) for $d_h = 20$ nm and 30 nm. Moreover, the strong SPhP mode is distributed in the HB characterized by both $\varepsilon_\perp < 0$ and $\varepsilon_\parallel < 0$ when $f = 0.1$ in Figs. 8(d)–8(f), and there is weak excitation of the HPPs mode in the HB where $\varepsilon_\perp < 0$ ($\varepsilon_\parallel > 0$) or $\varepsilon_\parallel < 0$ ($\varepsilon_\perp > 0$). Compared with Figs. 8(d) and 8(e), it is obvious that the excitation of SPhPs is much stronger in Fig. 8(f). When $f = 0.5$ in Figs. 8(g)–8(i), the overlapped SPhP mode appears at smaller transverse wavevectors when the thickness of the GaN films increases. It can be seen from Figs. 7 and 8 that the NFRHT within nanoporous GaN structures is primarily influenced by SPhP modes in the HB when altering the thickness of the GaN film from 10 nm to 30 nm.

Furthermore, we examine how the vacuum filling ratio influences NFRHT, considering a filling ratio range of 0 to 0.5, as discussed in Refs. [46,49]. Figure 9 illustrates the NFRHF in relation to the vacuum filling ratio for nanoporous GaN with various film thicknesses ($d_h = 10$ nm, $d_h = 50$ nm and $d_h = 100$ nm) at $d = 20$ nm. The highest $Q$ value of $9.31 \times 10^5$ W·m$^{-2}$ is attained in the nanoporous GaN for $d_h = 10$ nm when $f = 0.5$, while for $d_h = 50$ nm and $d_h = 100$ nm the maximum $Q$ values are $8.93 \times 10^5$ W·m$^{-2}$ and $8.90 \times 10^5$ W·m$^{-2}$, respectively, when $f = 0.2$.

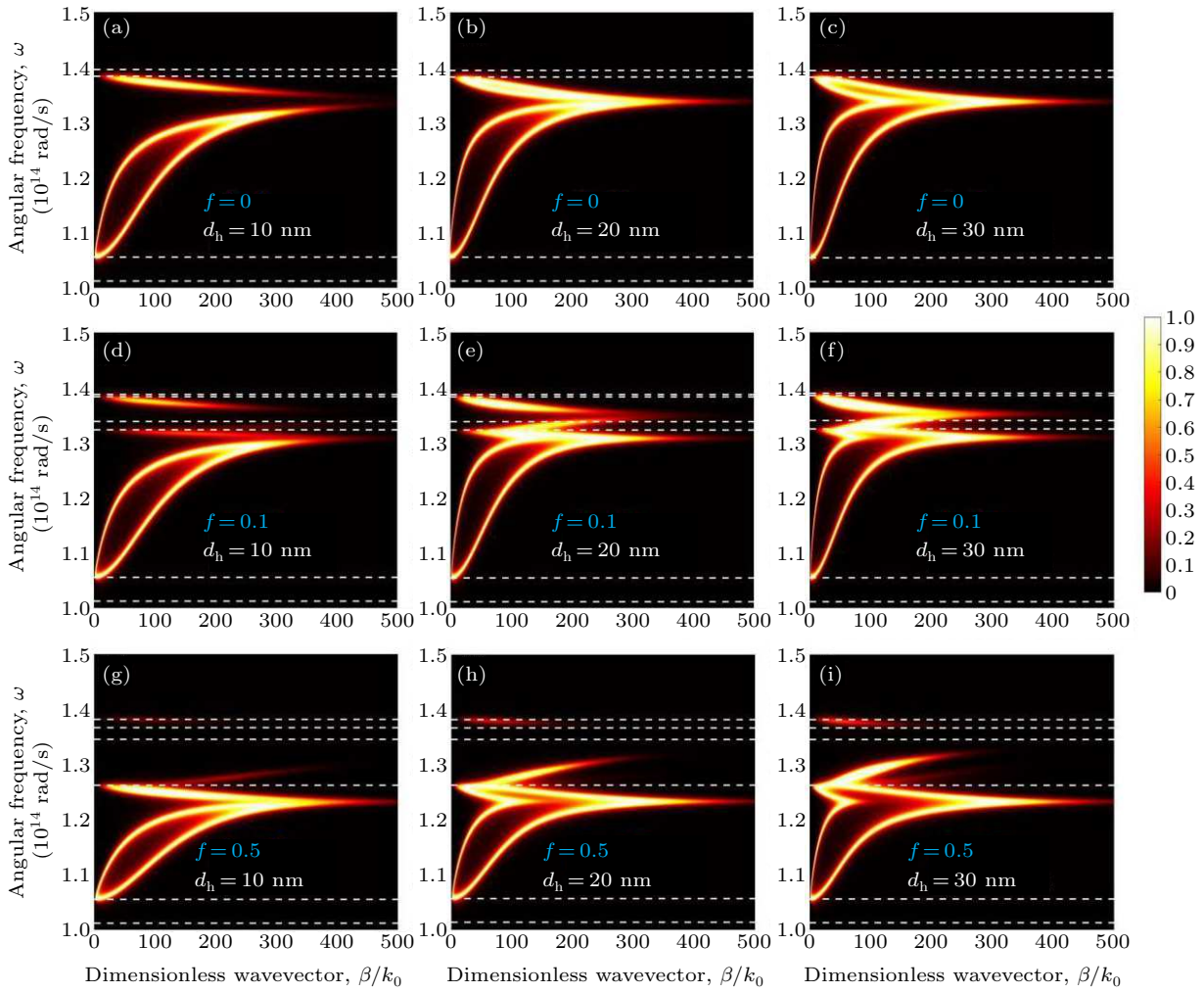



**Fig. 8.** Energy transmission coefficients of GaN and nanoporous GaN with $f = 0.1$ and $f = 0.5$ at $d_h = 10$ nm, $d_h = 20$ nm and $d_h = 30$ nm.

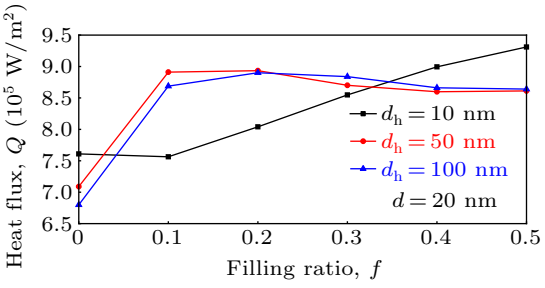



**Fig. 9.** Radiative heat flux as a function of vacuum filling ratio for nanoporous GaN with different film thicknesses ($d_h = 10$ nm, $d_h = 50$ nm and $d_h = 100$ nm) at $d = 20$ nm.

Investigating the impact of various filling ratios on NFRHF, we also present the SHF of nanoporous GaN with different filling ratios ($f = 0.2$, $f = 0.3$ and $f = 0.4$) at film thicknesses $d_h = 10$ nm, $d_h = 50$ nm and $d_h = 100$ nm (Fig. 10). It is noteworthy that the SHF of nanoporous GaN undergoes a redshift with increase in the filling ratio $f$. Specifically, considering the case of $d_h = 50$ nm, the nanoporous GaN structure with $f = 0.2$ reaches its peak value at $\omega = 1.29 \times 10^{14}$ rad·s$^{-1}$ in Fig. 10(a); the peak redshifts to $\omega = 1.27 \times 10^{14}$ rad·s$^{-1}$ when the vacuum filling ratio increases to $f = 0.3$ in Fig. 10(b) and continues to redshift at $\omega = 1.26 \times 10^{14}$ rad·s$^{-1}$ for $f = 0.4$

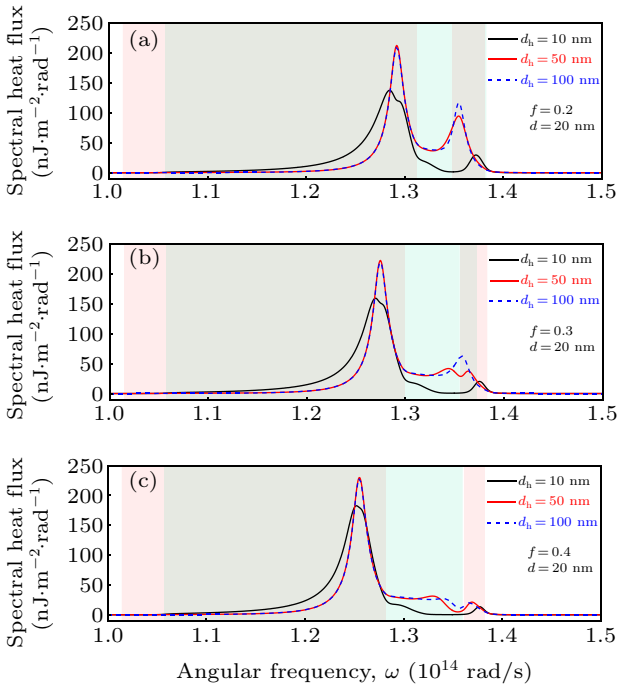



**Fig. 10.** SHF of the three configurations with different filling ratios ($f = 0.2$, $f = 0.3$ and $f = 0.4$) at film thicknesses $d_h = 10$ nm, $d_h = 50$ nm and $d_h = 100$ nm.

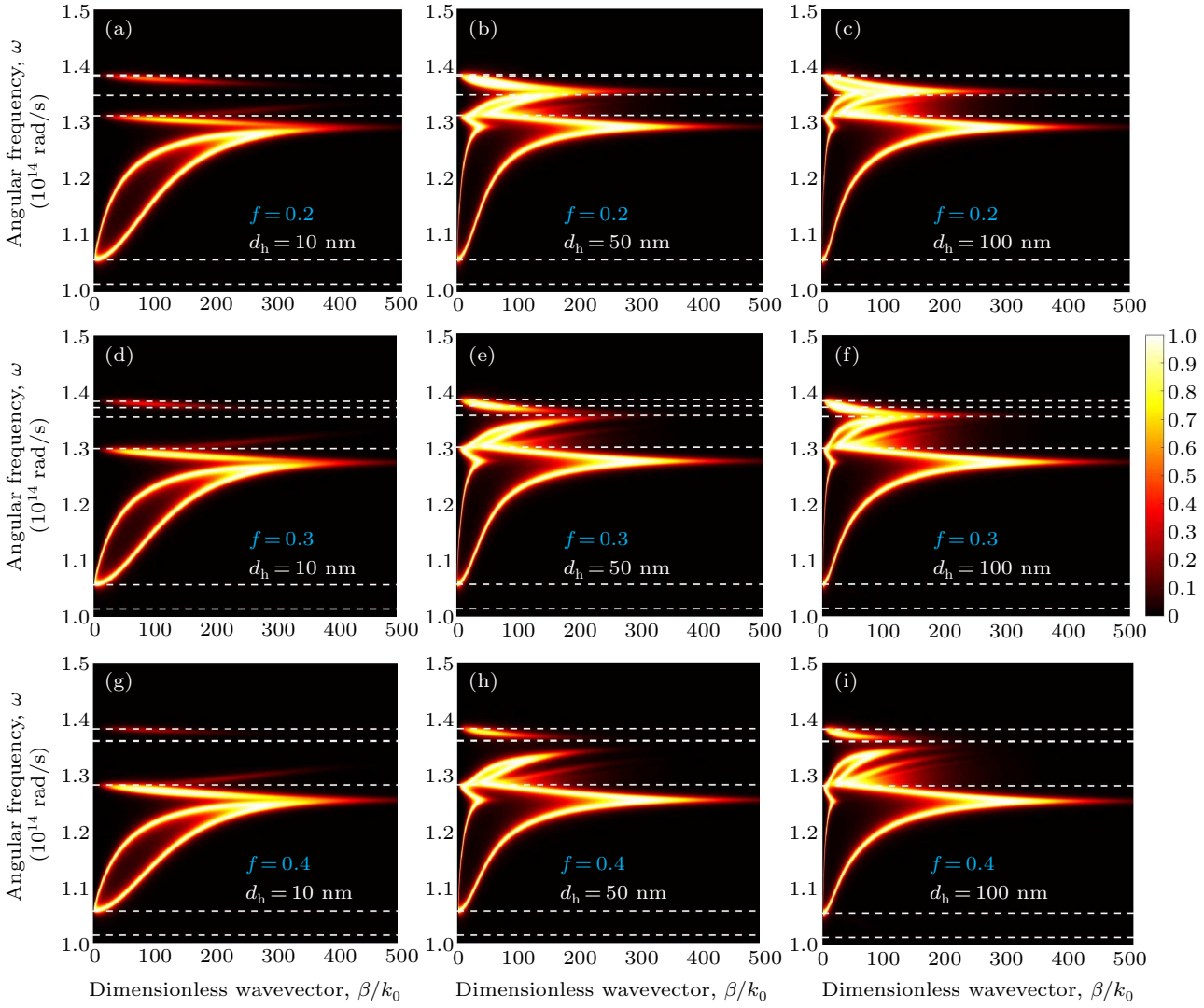



**Fig. 11.** Energy transmission coefficients of three nanoporous GaN structures with different filling ratios ($f = 0.2$, $f = 0.3$, $f = 0.4$) at $d_h = 10$ nm, $d_h = 50$ nm and $d_h = 100$ nm.

in Fig. 10(c). The redshift phenomenon, similar to the case of $d_h = 50$ nm, is observed in nanoporous GaN structures with $d_h = 10$ nm and $d_h = 100$ nm, as shown in Figs. 10(a)–10(c). Moreover, the SHF is predominantly concentrated in the HBs of both $\varepsilon_\perp < 0$ and $\varepsilon_\parallel < 0$, with comparatively lower values in the HB with $\varepsilon_\perp < 0$ ($\varepsilon_\parallel > 0$) or $\varepsilon_\parallel < 0$ ($\varepsilon_\perp > 0$).

The shift of the peak within the angular frequency region can be validated through the energy transmission coefficient. Figure 11 displays the energy transmission coefficients for nanoporous GaN with various filling ratios ($f = 0.2$, $f = 0.3$, $f = 0.4$) at $d_h = 10$ nm, $d_h = 50$ nm and $d_h = 100$ nm, respectively. As depicted in Figs.11(a), 11(d), and 11(f), it is evident that the prominent band corresponding to the excited SPhP modes redshifts to the lower angular frequency when $f$ increases from 0.2 to 0.4. Additionally, the excited SPhP mode with a large transverse wavevector, as illustrated in Fig. 11(b), undergoes a redshift to lower angular frequency in Fig. 11(e), and continues to redshift to a significantly lower angular frequency in Fig. 11(h) when $d_h = 50$ nm. The redshift phenomenon persists in Figs. 11(c), 11(f) and 11(i) with $d_h = 100$ nm. In addition, in Figs. 11(a)–11(c), 11(d)–11(f) and 11(g)–11(i), it is noticeable that the HPPs mode divides into multiple branches as the thickness of the GaN film increases from 10 nm to 100 nm.

To provide theoretical guidance for the wide application of nanoporous GaN in the field of NFRHT, we have further investigated the NFRHT between heterostructures of nanoporous GaN covered by graphene. G-GaN is composed of GaN and monolayer graphene, and G-nanoporous GaN consists of nanoporous GaN and monolayer graphene. Figure 12 shows the heat flux as a function of gap distance in G-GaN and G-nanoporous GaN for various vacuum filling ratios ($f = 0.1$–$0.5$). The results show that the NFRHF of all six structures decreases with increasing gap distance, and notably G-nanoporous GaN with $f = 0.5$ consistently exhibits the highest NFRHF. Specifically, at a gap distance of 10 nm, G-nanoporous GaN with vacuum filling ratios ranging from 0.1 to 0.5 exhibit NFRHF values of $5.28 \times 10^6$ W·m$^{-2}$,

$5.64 \times 10^6$ W·m$^{-2}$, $5.97 \times 10^6$ W·m$^{-2}$, $6.27 \times 10^6$ W·m$^{-2}$ and $6.43 \times 10^6$ W·m$^{-2}$, respectively, representing enhancement rates of 7.3%, 14.6%, 21.3%, 27.4% and 32.9% compared with the NFRHF of $4.92 \times 10^6$ W·m$^{-2}$ for G-GaN without nanopores. In addition, at a gap distance of 10 nm, the NFRHF in G-nanoporous GaN with $f = 0.5$ is greater than that of the nanoporous GaN without graphene by a factor of 1.86, demonstrating that the introduction of graphene can significantly enhance the NFRHT.

Figure 13 illustrates the variation in SHF for different samples, including G-GaN and G-nanoporous GaN with two different vacuum filling ratios (0.1 and 0.5) at $d = 10$ nm and $d = 50$ nm. Clearly, the SHF is distributed over a wide frequency region beyond the range of GaN HBs, owing to the introduction of graphene. Although the peaks of SHF in GaN HBs (shaded in colors) in Fig. 13 are much lower than in Fig. 4, the SHF supported by graphene is exhibited in a broader region, resulting in a higher heat flux in structures with graphene. Moreover, the SHF in GaN HBs exhibits higher peaks with increasing vacuum filling ratio in Figs. 13(a)–13(c), and SHF can be seen over a broader region of angular frequency (from $1.5 \times 10^{14}$ rad·s$^{-1}$ to $3.5 \times 10^{14}$ rad·s$^{-1}$), leading to a higher heat flux when the vacuum filling ratio increases. This is consistent with the results in Fig. 12. It can be seen by comparing the three structures that the peaks of SHF show blueshift (black lines in Fig. 13(a), red lines in Fig. 13(b), blue lines in Fig. 13(c)), as the filling ratio increases. Specifically, when $d = 10$ nm, the highest peak in G-GaN is located at $1.73 \times 10^{14}$ rad·s$^{-1}$, while in G-nanoporous GaN with $f = 0.1$ it is situated at $1.76 \times 10^{14}$ rad·s$^{-1}$ and in G-nanoporous GaN with $f = 0.5$ the peak shifts to $1.91 \times 10^{14}$ rad·s$^{-1}$. When $d = 50$ nm, the SHF drops sharply in comparison with that for $d = 10$ nm, and a similar blueshift of the highest peak occurs.

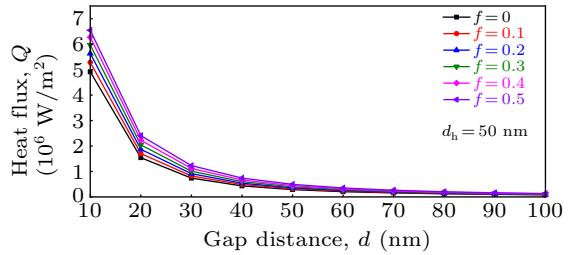



**Fig. 12.** Radiative heat flux as a function of gap distance for G-GaN and G-nanoporous GaN with different vacuum filling ratios ($f = 0.1$–$0.5$) at $\mu = 0.1$ eV and $d_h = 50$ nm.

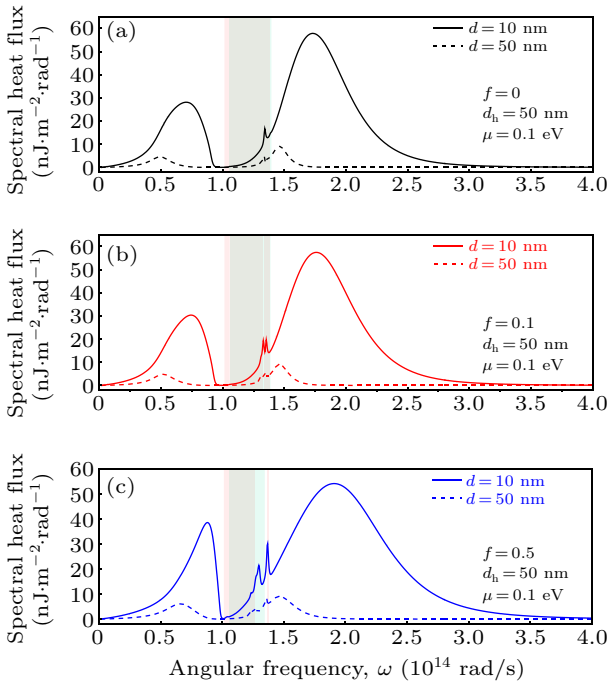



**Fig. 13.** SHF of G-GaN and G-nanoporous GaN with $f = 0.1$ and $f = 0.5$ at $d = 10$ nm and $d = 50$ nm.

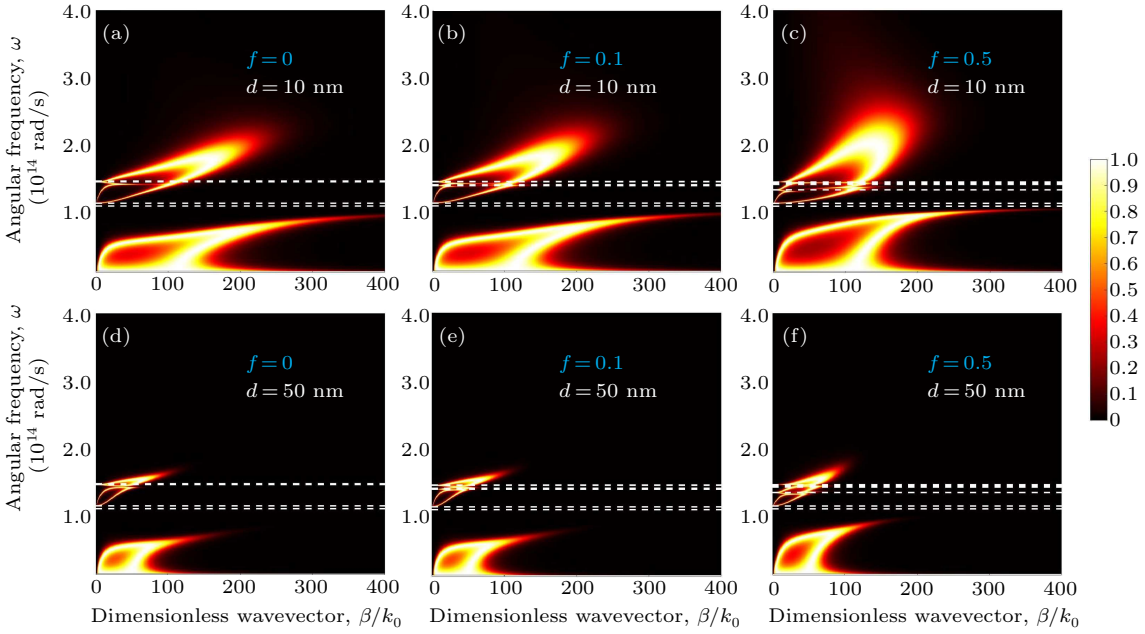



**Fig. 14.** Energy transmission coefficients of G-GaN and G-nanoporous GaN with $f = 0.1$ and $f = 0.5$ at $d = 10$ nm and $d = 50$ nm.

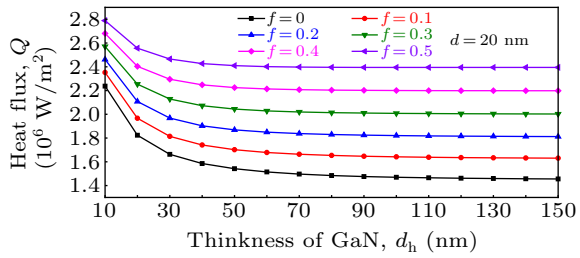



**Fig. 15.** Radiative heat flux as a function of thickness of GaN film for G-GaN and G-nanoporous GaN with different vacuum filling ratios ($f = 0.1$–$0.5$) at $d = 20$ nm and $\mu = 0.1$ eV.

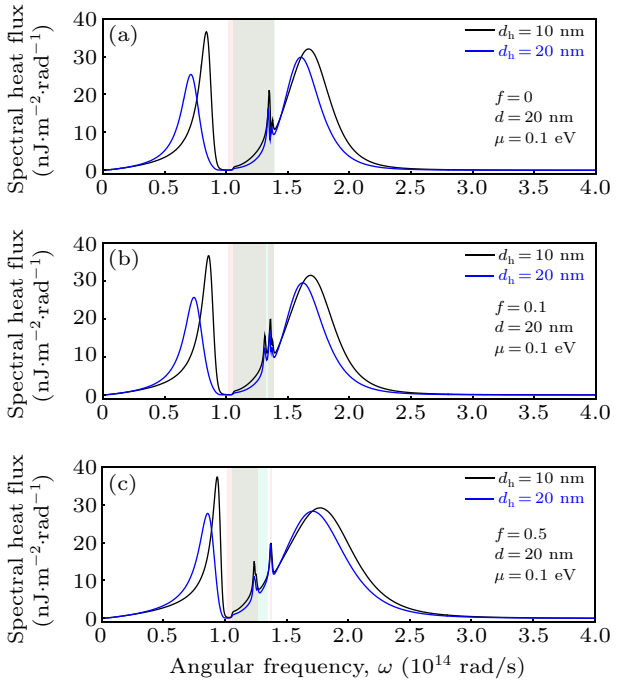



**Fig. 16.** SHF of G-GaN and G-nanoporous GaN with $f = 0.1$ and $f = 0.5$ at $d_h = 10$ nm and $d_h = 20$ nm.

Figure 14 shows the energy transmission coefficients of G-GaN as well as G-nanoporous GaN with $f = 0.1$ and $f = 0.5$, when $d = 10$ nm and $d = 50$ nm. The presence of graphene leads to the generation of SPP modes outside the HBs of GaN. In the frequency range of $1.0 \times 10^{14}$ rad·s$^{-1}$ to $4.0 \times 10^{14}$ rad·s$^{-1}$, increasing the vacuum filling ratio leads to a stronger coupling mode that blueshifts towards higher angular frequencies, which agrees well with the blueshift of the SHF shown in Figs. 14(a)–14(c) and 14(d)–14(f). Compared with the energy transmission coefficients in Fig. 5, the SPhP modes excited in the HBs are largely suppressed, which explains the much lower peaks of SHF shown in Fig. 14 compared with that shown in Fig. 4. As the gap distance increases from 10 nm to 50 nm, the bright area reduces in Figs. 14, leading to the sharp drop of SHF (solid and dotted lines in Fig. 14).

The thickness of GaN film generally affects the NFRHF. Figure 15 demonstrates how the NFRHF varies with the thickness of GaN film for both G-GaN and G-nanoporous GaN characterized by different vacuum filling ratios ($f = 0.1$–$0.5$) at a fixed $d = 20$ nm and $\mu = 0.1$ eV. The NFRHF consistently decreases with increasing thickness of the GaN film, and the G-nanoporous GaN sample with $f = 0.5$ exhibits superior NFRHF performance, as shown in Fig. 15. The NFRHF of G-GaN experiences a rapid decline, decreasing monotonically from $2.24 \times 10^6$ W·m$^{-2}$ ($d_h = 10$ nm) to $1.46 \times 10^6$ W·m$^{-2}$ ($d_h = 150$ nm), resulting in a suppression rate of 34.8%. To be more specific, for G-nanoporous GaN with $f = 0.1$, the NFRHF shows a decrease from $2.35 \times 10^6$ W·m$^{-2}$ ($d_h = 10$ nm) to $1.63 \times 10^6$ W·m$^{-2}$ ($d_h = 150$ nm), resulting in a suppression rate of 30.6%. Similarly, for G-nanoporous GaN with $f = 0.5$, the NFRHF exhibits a gradual decline, ranging from $2.79 \times 10^6$ W·m$^{-2}$ ($d_h = 10$ nm) to $2.39 \times 10^6$ W·m$^{-2}$ ($d_h = 150$ nm), with a suppression rate of 14.3%.

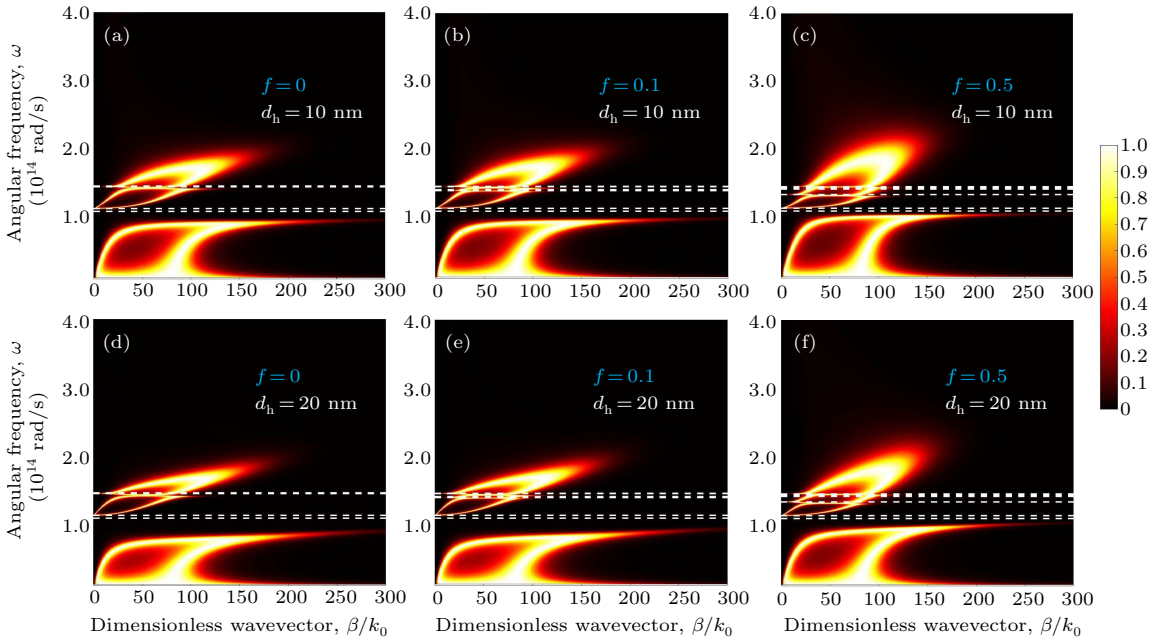



**Fig. 17.** Energy transmission coefficients of G-GaN and G-nanoporous GaN configurations with $f = 0.1$ and $f = 0.5$ at $d_h = 10$ nm and $d_h = 20$ nm.

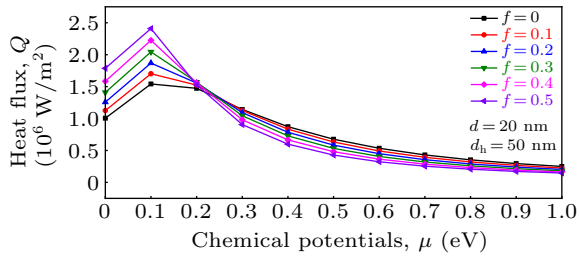



**Fig. 18.** Radiative heat flux as a function of chemical potential of graphene for G-GaN and G-nanoporous GaN with different vacuum filling ratios ($f = 0.1$–$0.5$) at $d = 20$ nm and $d_h = 50$ nm.

Figure 16 illustrates the SHF of G-GaN and G-nanoporous GaN with $f = 0.1$ and $f = 0.5$ when $d_h = 10$ nm and $d_h = 20$ nm. It is clear that SHF decreases when thickness of the GaN film increases from 10 nm to 20 nm. Specifically, the peak becomes lower and wider in the frequency range $0.5 \times 10^{14}$ rad·s$^{-1}$ to $1.0 \times 10^{14}$ rad·s$^{-1}$, and the peak is lower and narrower in the frequency range $1.5 \times 10^{14}$ rad·s$^{-1}$ to $2.0 \times 10^{14}$ rad·s$^{-1}$.

In order to further investigate the underlying physical mechanisms, figure 17 shows the energy transmission coefficients for G-GaN and two G-nanoporous GaN samples with $f = 0.1$ and $f = 0.5$ when $d_h = 10$ nm and $d_h = 20$ nm. Comparing Fig. 17(a) with Fig. 17(d), a slight decrease in area of the bright region can be found from $1.0 \times 10^{14}$ rad·s$^{-1}$ to $2.0 \times 10^{14}$ rad·s$^{-1}$, which results in the variation of SHF shown in Fig. 16(a). Similar phenomena can be observed in Figs. 17(b), 17(e) and 17(c), 17(f), that leads to similar changes of SHF shown in Figs. 16(b) and 16(c).

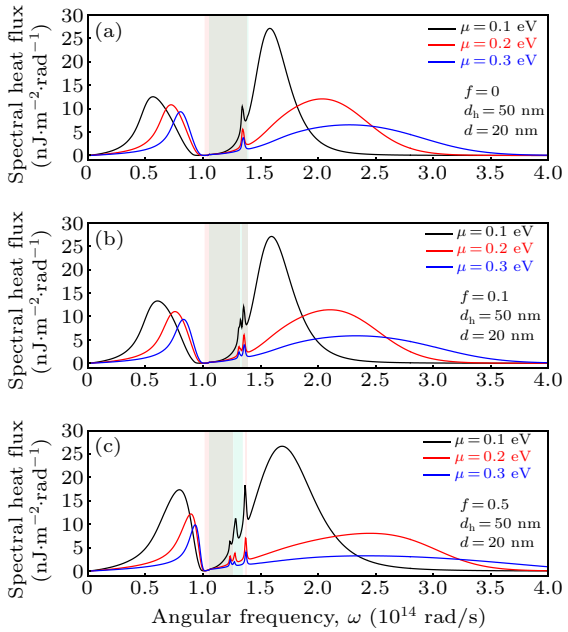



**Fig. 19.** SHF of G-GaN and G-nanoporous GaN with $f = 0.1$ and $f = 0.5$ at $d_h = 50$ nm and $d = 20$ nm.

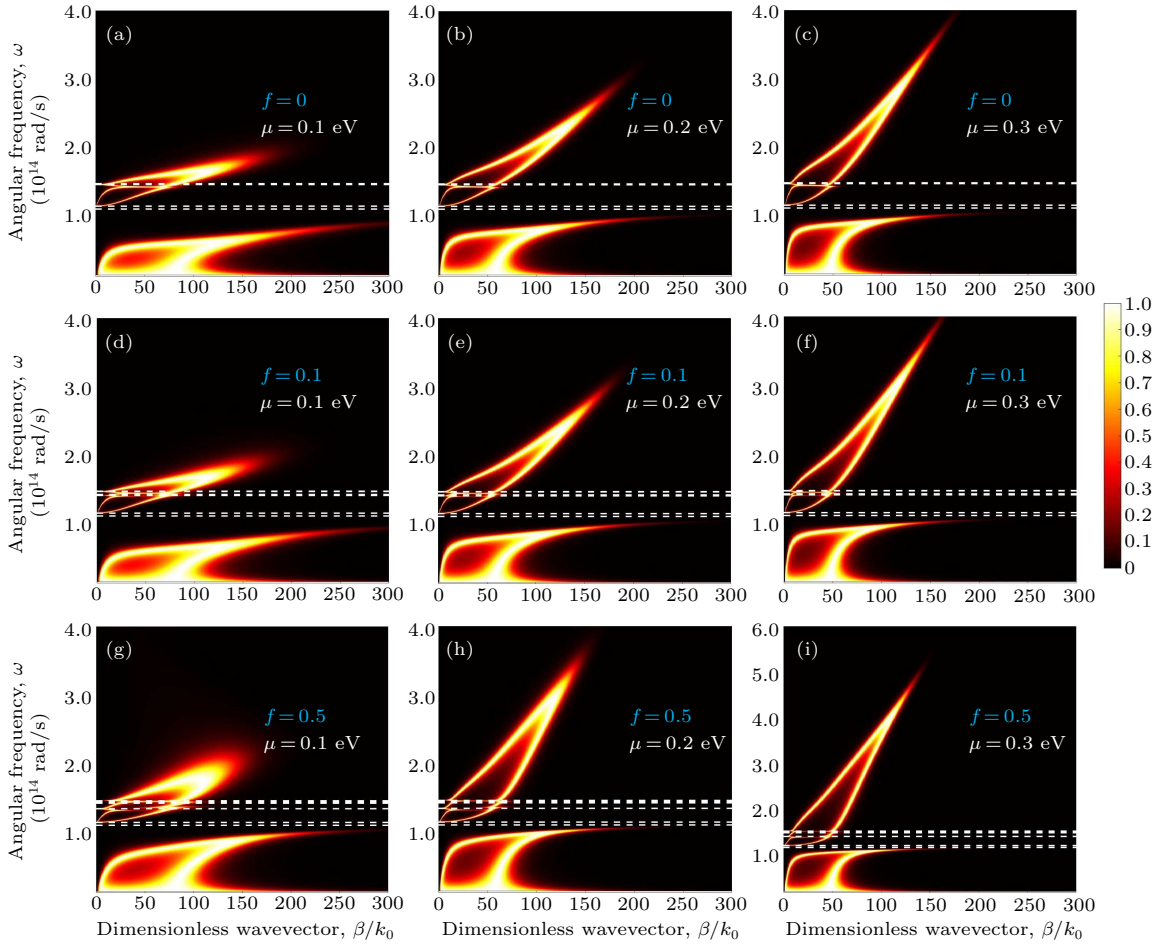



**Fig. 20.** Energy transmission coefficients of G-GaN and G-nanoporous GaN with $f = 0.1$ and $f = 0.5$ at $\mu = 0.1$ eV, $\mu = 0.2$ eV and $\mu = 0.3$ eV.

The chemical potential of graphene generally affects the NFRHF. Figure 18 illustrates the NFRHF as a function of the chemical potential of graphene in G-GaN and G-nanoporous GaN with various vacuum filling ratios ($f = 0.1$–$0.5$) at $d =$ 20 nm and $d_h = 50$ nm. It can be observed that the NFRHF of all six samples exhibits an initial increase followed by a decrease as the chemical potential of graphene increases, with maximum NFRHF values occurring at $\mu = 0.1$ eV. When $\mu = 0.1$ eV, the NFRHF of G-nanoporous GaN with $f = 0.1$ and $f = 0.5$ reaches $1.70 \times 10^6$ W·m$^{-2}$ and $2.41 \times 10^6$ W·m$^{-2}$, respectively, which are 10.4% and 56.5% higher than for G-GaN ($1.54 \times 10^6$ W·m$^{-2}$). It is worth noting that when the chemical potential of graphene is less than 0.2 eV, a higher vacuum filling ratio will lead to a more pronounced enhancement of NFRHF. When $\mu > 0.2$ eV, an increase in the vacuum filling ratio leads to a decrease of NFRHF.

Figure 19 shows the SHF of G-GaN and G-nanoporous GaN with $f = 0.1$ and $f = 0.5$ at $\mu = 0.1$ eV, $\mu = 0.2$ eV and $\mu = 0.3$ eV. The results in Fig. 19 demonstrate that the SHF at $\mu = 0.1$ eV has the highest peak value and occupies the most extensive area within the angular frequency, indicating superior performance in enhancing NFRHT. In Fig. 19(a), as the chemical potential of graphene increases the SHF peak undergoes a slight blueshift while simultaneously decreasing in magnitude in the HBs. In particular, at $\mu = 0.1$ eV, G-GaN reaches the highest peak value at $\omega = 1.341 \times 10^{14}$ rad·s$^{-1}$; the peak blueshifts towards $\omega = 1.345 \times 10^{14}$ rad·s$^{-1}$ as chemical potential of graphene increases to $\mu = 0.2$ eV and further blueshifts to $\omega = 1.349 \times 10^{14}$ rad·s$^{-1}$ at $\mu = 0.3$ eV. A similar phenomenon can also be found in G-nanoporous GaN with $f = 0.1$ and $f = 0.5$, as illustrated in Figs. 19(b) and 19(c).

Furthermore, figrue 20 shows the energy transmission coefficients for both G-GaN and G-nanoporous GaN with filling ratios of $f = 0.1$ and $f = 0.5$ and chemical potentials $\mu = 0.1$ eV, $\mu = 0.2$ eV and $\mu = 0.3$ eV. Primarily, as the chemical potential of graphene increases in Fig. 20 (from (a) to (c)), the SPPs associated with graphene become progressively confined to a narrower wave vector space with the transverse component $\beta$ of the wave vector within the bright band shrinking from $300k_0$ to $200k_0$; thus the configurations reach the optimal NFRHF at $\mu = 0.1$ eV. Moreover, the SPP mode of graphene exhibits a broader region of angular frequency in the high-frequency regime, where the excited SPP mode covers $2.0 \times 10^{14}$ rad·s$^{-1}$ to $4.0 \times 10^{14}$ rad·s$^{-1}$. As a consequence, the blueshift of the SHF peak depicted in Fig. 19 is observed.

## 4. Conclusion

In this paper we have investigated NFRHT for bare nanoporous GaN and nanoporous GaN covered by graphene and analyzed the effects of gap distance $d$, GaN film thickness $d_h$ and vacuum filling ratio $f$ on NFRHT. The results show that the NFRHF decreases as the gap distance increases, and the difference between different structural configurations is more obvious at smaller gap distances. Compared with GaN without nanopores, the NFRHT of nanoporous GaN with $f = 0.1$ and $f = 0.5$ can be effectively improved by introducing a vacuum when the GaN film thickness increases. Redshifts of SHF are identified and analyzed by the excitation of SPhPs through energy transmission coefficients. In addition, NFRHT of nanoporous GaN can be enhanced by covering with monolayer graphene. With increase in the vacuum filling ratio, blueshifts of SHF are observed and analyzed by the excitation of SPPs through energy transmission coefficients. Based on the above results, this paper provides a theoretical basis for the development and design of thermal radiation micro–nano devices with nanoporous GaN. This work will promote potential applications of nanoporous materials in thermal modulators, energy harvesting and thermal management.

## Acknowledgments

Project supported by the National Natural Science Foundation of China (Grant No. 52106099), the Natural Science Foundation of Shandong Province (Grant No. ZR2022YQ57), and the Taishan Scholars Program.

## References

[1] Shi K Z, Bao F L and He S L 2017 *ACS Photonics* **4** 971
[2] Zhao B, Guizal B, Zhang Z M, Fan S H and Antezza M 2017 *Phys. Rev. B* **95** 245437
[3] Shi K Z, Liao R, Cao G J, Bao F L and He S L 2018 *Opt. Express* **26** A591
[4] Liu H T, Shi K Z, Zhou K, Ai Q, Xie M and Wu X H 2023 *Int. J. Heat Mass Transfer* **208** 124081
[5] Laura R G, Dakotah T, Rohith M, Nicolas A, Edgar M and Pramod R 2022 *Phys. Rev. Lett.* **129** 145901
[6] Kralik T, Hanzelka P, Zobac M, Musilova V, Fort T and Horak M 2012 *Phys. Rev. Lett.* **109** 224302
[7] Salihoglu H and Xu X F 2019 *J. Quant. Spectrosc. Radiat. Transf.* **222–223** 115
[8] Zhou C L, Zhang Y and Yi H L 2022 *Langmuir* **38** 7689
[9] Wang B, Zhang J H and Li C Y 2022 *Results Phys.* **33** 105199
[10] Sun Y S, Hu Y, Shi K Z, Zhang J H, Feng D D and Wu X H 2022 *Phys. Scr* **97** 095506
[11] He M J, Qi H, Ren Y T, Zhao Y J and Antezza M 2020 *Int. J. Heat Mass Transfer* **150** 119305
[12] Zhang Y, Yi H L and Tan H P 2018 *ACS Photonics* **5** 3739
[13] Yang J, Du W, Su Y S, Fu Y, Gong S X, He S L and Ma Y G 2018 *Nat. Commun.* **9** 4033
[14] Wu H H, Huang Y, Cui L J and Zhu K Y 2019 *Phys. Rev. Appl.* **11** 054020
[15] Hu Y, Sun Y S, Zheng Z H, Song J L, Shi K Z and Wu X H 2022 *Int. J. Heat Mass Transfer* **189** 122666
[16] Zhou C L, Wu X H, Zhang Y and Yi H L 2021 *Int. J. Heat Mass Transfer* **180** 121794
[17] Wu X H and Fu C J 2021 *Int. J. Heat Mass Transfer* **168** 120908
[18] Wu X H, Fu C J and Zhang Z M 2020 *J. Heat Transfer* **142** 072802
[19] Wu X H and Liu R Y 2020 *ES Energy Environ.* **10** 66
[20] Shi K Z, Chen Z Y, Xu X N, Evans J L and He S L 2021 *Adv. Mater.* **33** 2106097
[21] Liu R Y, Zhou C L, Zhang Y, Cui Z, Wu X H and Yi H L 2022 *Int. J. Extrem. Manuf.* **4** 032002
[22] Wu X H and Fu C J 2021 *J. Quant. Spectrosc. Radiat. Transf.* **258** 107337

[23] Yu K, Li L, Shi K Z, Liu H T, Hu Y, Zhang K H, Liu Y F and Wu X H 2023 *Int. J. Heat Mass Transfer* **211** 124229
[24] Zhang J H, Yang B, Shi K Z, Liu H T and Wu X H 2023 *Nanophotonics* **12** 1833
[25] Kan Y H, Zhao C Y and Zhang Z M 2020 *Phys. Rev. Appl.* **13** 014069
[26] Zhang J H, Liu H T, Zhang K H, Cao J C and Wu X H 2023 *Int. J. Heat Mass Transfer* **202** 123714
[27] Liu X L, Wang L P and Zhang Z M 2015 *Nanoscale Microscale Thermophys. Eng.* **19** 98
[28] Liu X L and Zhang Z M 2015 *Appl. Phys. Lett.* **107** 143114
[29] Basu S, Chen Y B and Zhang Z M 2007 *Int. J. Energy Res.* **31** 689
[30] Messina R and Ben-Abdallah P 2013 *Sci. Rep.* **3** 1383
[31] Guha B, Otey C, Poitra C B, Fan S H and Lipson M 2012 *Nano Lett.* **12** 4546
[32] Zhao D L, Aili A, Zhai Y, Lu J T, Kidd D, Tan G, Yin X B and Yang R G 2019 *Joule* **3** 111
[33] Cai L L, Song A Y, Li W, Hsu P C, Lin D C, Catrysse P B, Liu Y Y, Peng Y C, Chen J, Wang H X, Xu J W, Yang A K, Fan S H and Cui Y 2018 *Adv. Mater.* **30** 1802152
[34] Inoue T, Koyama T, Kang D D, Ikeda K, Asano T and Noda S 2019 *Nano Lett.* **19** 3948
[35] Cakiroglu D, Perez J P, Evirgen A, Lucchesi C, Lucchesi P O, Taliercio T, Tournie E and Vaillon R 2019 *Sol. Energy Mater. Sol. Cells* **203** 110190
[36] Inoue T, Ikeda K, Song B, Suzuki T, Ishino K, Asano T and Noda S 2021 *ACS Photonics* **8** 2466
[37] Lucchesi C, Cakiroglu D, Perez J P, Taliercio T, Tournie E, Chapuis P O and Vaillon R 2021 *Nano Lett.* **21** 4524
[38] Biehs S A, Rosa F S S and Ben-Abdallah P 2011 *Appl. Phys. Lett.* **98** 243102
[39] Biehs S A, Menon V M and Agarwal G S 2016 *Phys. Rev. B* **93** 245439
[40] Lang S, Tschikin M, Biehs S A, Petrov A Y and Eich M 2014 *Appl. Phys. Lett.* **104** 121903
[41] Lang S, Lee H S, Petrov A Y, Stormer M, Ritter M and Eich M 2013 *Appl. Phys. Lett.* **103** 021905
[42] Xu D Y, Bilal A, Zhao J M, Liu L H and Zhang Z M 2019 *Int. J. Heat Mass Transfer* **142** 118432
[43] Xu D Y, Zhao J M and Liu L H 2021 *Appl. Phys. Lett.* **119** 141106
[44] Zhou C L, Yang S H, Zhang Y and Yi H L 2020 *Nanoscale Microscale Thermophys. Eng.* **24** 168
[45] Zhou C L, Zhang Y and Yi H L 2022 *Mat. Today Phys.* **28** 100891
[46] Biehs S A, Ben-Abdallah P, Rosa F S S, Joulain K and Greffet J J 2011 *Opt. Express* **19** A1088
[47] Liu X L, Zhang R Z and Zhang Z M 2014 *Int. J. Heat Mass Transfer* **73** 389
[48] Hong X J, Li J W, Wang T B, Zhan D J, Liu W X, Liao Q H, Yu T B and Liu N H 2018 *Jpn. J. Appl. Phys.* **57** 045001
[49] Li X H, Wang T B, Yu T B and Liao Q H 2022 *Eur. Phys. J. B* **95** 140
[50] Beeler M, Trichas E and Monroy E 2013 *Semicond. Sci. Technol.* **28** 074022
[51] Baliga B J 2013 *Semicond. Sci. Technol.* **28** 074011
[52] S Chowdhury, Swenson B L, Wong M O and Mishra U K 2013 *Semicond. Sci. Technol.* **28** 074014
[53] Cheah S F, Lee S C, Ng S S, Yam F K, Abu Hassan H and Hassan Z 2015 *J. Lumin.* **159** 303
[54] Didari A, Elçioğlu E B, Okutucu-Özyurt T and Mengüç M P 2018 *J. Quant. Spectrosc. Radiat. Transf.* **212** 120
[55] Yan H G, Li X S, Chandra B, Tulevski G, Wu Y Q, Freitag M, Zhu W J, Avouris P and Xia F N 2012 *Nat. Nanotechnol.* **7** 330
[56] Yan J, Zhang Y B, Kim P and Pinczuk A 2007 *Phys. Rev. Lett.* **98** 166802
[57] Ng S S, Hassan Z and Abu Hassan H 2008 *Solid State Commun.* **145** 535
[58] Pandey A, Kumari M and Raman R 2021 *Optik* **225** 165834
[59] Ng S S, Yoon T L, Hassan Z and Abu Hassan H 2009 *Appl. Phys. Lett.* **94** 241912
[60] Torii K, Koga T, Sota T, Azuhata T, Chichibu S F and Nakamura S 2000 *J. Phys. Condens. Matter* **12** 7041
[61] G Yu, Rowell N L and Lockwood D J 2004 *J. Vac. Sci. Technol. A* **22** 1110
[62] Biehs S A, Tschikin M and Ben-Abdallah P 2012 *Phys. Rev. Lett.* **109** 104301
[63] Liu X L, Bright T J and Zhang Z M 2014 *J. Heat Transfer* **136** 092703
[64] Lim M, Lee S S and Lee B J 2013 *Opt. Express* **21** 22173
[65] Saarinen J J and Sipe J E 2008 *J. Mod. Optic.* **55** 13